Received 28 March 2023; revised 21 May 2023; accepted 3 June 2023. Date of publication 12 June 2023; date of current version 29 June 2023.

Digital Object Identifier 10.1109/OJAP.2023.3285233

Physics-Based Coherent Modeling of Long-Range Millimeter-Wave Propagation and Scattering in Rain

BEHZAD YEKTAKHAH (Member, IEEE), AND KAMAL SARABANDI (Life Fellow, IEEE)

Department of Electrical Engineering and Computer Science, University of Michigan at Ann Arbor, Ann Arbor, MI 48103, USA

CORRESPONDING AUTHOR: B. YEKTAKHAH (e-mail: byekta@umich.edu)

ABSTRACT Precipitation and in particular rain present a random medium with constituent particles having dimensions comparable to the wavelength at millimeter-wave frequencies. Due to considerable scattering of waves from such particles, significant signal attenuation and phase front aberration can take place which are important factors that must be considered in modern communication system or radar design. This paper presents a fast and accurate numerical method for phase coherent modeling of wave propagation and scattering in random media, like rain. In this approach, the random medium is divided into sufficiently large finite slabs and each slab is modeled as a network with multiple input/output ports where ports represent rays with different polarizations propagating in different directions entering and leaving the slabs. The cascaded networks of slabs can be used to find the response of the random medium to any arbitrary source. The proposed method considers multiple scattering among all scatterers and thus the entire physics of wave-particle interactions is accounted for. In addition, the method can model both the mean and the fluctuating parts of waves in the random medium. To demonstrate the applicability of the proposed method, it is used for the calculation of the specific attenuation in rain media as a function of rain rates and frequency within the millimeter-wave band. The results show a good match with the available rain attenuation data in the literature.

INDEX TERMS Communication system, millimeter-wave, radar, rain, random media, specific attenuation.

I. INTRODUCTION

THE WIDE spectrum available at the millimeter-wave (mm-wave) band is the main reason for the development of the future high data rate wireless communication systems (such as 5G) [1] and Internet of Things (IoT) [2]. The small wavelength at mm-wave frequencies and low atmospheric absorption at frequencies around 77 GHz enable design of high resolution short and long-range radars with compact form factor for industrial applications (such as storage tank level measurement) and future advanced driver-assistance systems (ADAS). In automotive industry, radars are key sensors [3] that provide target position and velocity with high accuracy in addition to being able to operate in inclement weather conditions with a much lower cost compared to LIDAR. Efforts are being made to introduce higher mm-wave frequencies for automotive radars to reduce size and/or improve resolution to be competitive with LIDAR resolution [4], [5].

With short wavelengths, ranging from 1 mm to 10 mm, waves at mm-wave frequencies exhibit higher interactions with the objects in the environment and thus the propagation characteristics at mm-wave frequencies are significantly different from those at lower frequencies (the microwave band and lower) in terms of path loss, foliage loss, phase aberration, and diffraction [6], [7], [8], [9]. This can pose many challenges in design of mm-wave communication and radar systems. While the free space path loss can be compensated by utilizing higher gain antennas, the propagation loss due to rain, foliage, and the resulting aberration in phase front must be carefully considered in design of mm-wave systems. This is more critical in case of non-line-of-sight links in cluttered environments such as in urban areas [10]. Various empirical models have been proposed for estimating attenuation of mm-waves in line-of-sight and non-line-of-sight propagation in urban areas [11], [12]. In case of attenuation through rain, several measurement results have been reported for various

rain rates at different frequencies [13], [14]. These results are used for design of mm-wave communication systems. In mm-wave radar design, specifically in coherent systems such as synthetic aperture and MIMO radars, in addition to the attenuation, the phase fluctuation of the received signal in rain across the antenna array plays an important role for accurate modeling of the radar performance in the presence of rain.

Rain can be viewed as a discrete random medium consisting of particles of different sizes with a distribution function that depends on the rain rate. The size distribution of rain droplets is described by well-known models such as Marshall-Palmer [15] and gamma distribution [16]. Due to high dielectric constant of water and the size of the droplets that can be a considerable fraction of wavelength, a strong scattering can occur in the medium. The strong scattering from particles results in significant attenuation, absorption, and phase aberration due to multiple scattering. Thus, the received signal propagated through rain has random phase and amplitude fluctuation which can be decomposed into two components: a) the mean field which accounts for the average attenuation through the rain and b) fluctuating or incoherent part that accounts for the phase and amplitude fluctuations in the received signal. Several models have been developed to model the mean and the fluctuating parts of the fields at different frequency ranges and for different types of random media [17], [18], [19], [20]. For modeling of the mean field, dielectric mixing formula can be used at low frequencies to model the random medium as an effective medium. In case of week permittivity fluctuations, perturbation techniques such as Born approximation can be used. In case of sparse discrete random media, methods based on single scattering approximation such as Foldy's method [17] have been developed.

For modeling the fluctuating part of the field, radiative transfer (RT) theory and T-matrix method can be applied. RT method is applicable to sparse discrete random media and is based on the law of conservation of energy and single scattering approximation [18]. In [19], a method based on ABCD-matrix is developed for analysis of propagation (including phase information) in 2D periodic random media. Full-wave T-matrix method can provide phase information of the waves; however, it is only applicable to small 3D problems involving small number of particles. T-matrix method applicability also depends on the volume fraction of the random medium. A discussion of T-matrix method limitation in 3D problems can be found in [20]. In [21], a Monte Carlo technique was presented for analyses of multi-scattering in rain considering spherical shape for rain particles and excluding the phase and polarization information of waves.

For long propagation through rain, multiple scattering effects become significant and single scattering approximation such as Foldy's method can only provide an upper limit for the specific attenuation. In addition, the single scattering model is valid only in short range propagation where the mean field is dominant. It is shown in [22], [23] that after a certain range, the fluctuating part of the field becomes dominant that invalidates the specific attenuation predicted by single scattering approximation. This shows the need for a better technique to accurately predict the mean and fluctuating parts of fields propagating in rain and experiencing multiple scattering.

In [23], propagation and scattering in a 2-D random medium is modeled by a scattering matrix (S-matrix) to find the specific attenuation over long propagation distance in spectral domain. In this method, first, the random medium is divided into slabs and then each slab, similar to a network with multiple ports, is described by an S-matrix. Then, the S-matrices of different slabs are cascaded to obtain an S-matrix representing the whole random medium.

This paper extends the idea of S-matrix method to 3-D random media to analyze coherent wave propagation and scattering at mm-wave band in rainy atmosphere. The method considers multiple scattering and provides amplitude and phase data for both forward propagating and backscattered waves for arbitrary sources and thus eliminating the need for full wave simulations which is not possible for very large propagation and scattering problems. In the method, the random medium is divided into slabs with a certain thickness and for each slab, the input and output wave fronts at two interfaces of the slab are represented by the superposition of plane waves with different polarizations and propagating in different directions. Each plane wave specifies a port for the slab equivalent network. Then, the S-matrix is defined to relate the amplitude/phase of each output port to the amplitude/phase of all input ports at both interfaces. Then the S-matrices of different slabs are cascaded to calculate scattering from and propagation through the random medium (including the phase information) for any source. This way multiple scattering among scatterers in different slabs are taken into consideration. This model is used to calculate the specific attenuation of mm-wave signals as a function of rain rate and frequency over long distances. The simulations are performed for different rain rates, ranging from few mm/hr to tens of mm/hr, within the frequency range from 28 GHz (5G) to 230 GHz. Comparison of the simulation results with the data available in literature shows the accuracy of the presented method.

S-matrix method is a general method that can be applied to any dense/sparse random media. In this paper, rain media is selected to demonstrate the capability of S-matrix method, since rain media have been thoroughly studied and various empirical models and measurement data are available for propagation and scattering in rain at different frequency bands. Other examples of the applicability of the method are analysis of propagation and scattering in foliage, sandstorm (useful in applications such as radar imaging, target acquisition, and helicopter landing [9]), as well as cloud/fog or murky water at optical frequencies.

The advantages of the S-matrix method are: 1) it is based on full-wave analysis; 2) it is applicable to dense or sparse random media; 3) it tracks the polarization of the wave

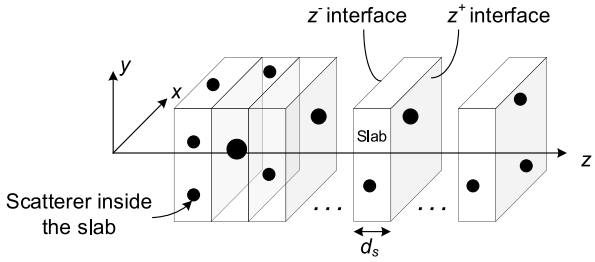

FIGURE 1. Random medium layered in *z*-direction.

along the propagation; 4) it tracks phase aberration to the phase front needed for assessing the performance of coherent imaging systems (such as SAR or MIMO radars) operating in random media; 5) it can be used for random media with scatterers having arbitrary shapes.

This paper is organized as follows. In Section II, the method based on the S-matrix extended to 3-D is introduced. Calculation of the elements of S-matrix is detailed in Section III. S-matrix simulation results for rain are given in Section IV and compared to the available data in literature. Concluding remarks are given in Section V.

II. 3-D S-MATRIX METHOD

The first step in S-matrix method is to divide the random medium to multiple slabs with a certain thickness as shown in Fig. 1. In this paper, the direction of propagation is assumed to be in z-direction and the random medium is divided along the direction of propagation into N_s slabs and slabs' interfaces are parallel to xy-plane. The interface with larger z-position value is denoted by z^+ and the other one is denoted by z^- (Fig. 1). The time dependency of waves is $e^{j\omega t}$.

At the two interfaces of each slab, the incoming and outgoing electric field waves are first expanded by plane waves traveling in different directions. Electric field vector can be represented by infinite number of plane waves as:

$$\overline{E}(x,y,z)=\frac{1}{4\pi^2}\int_{-\infty}^{+\infty}\int_{-\infty}^{+\infty}\overline{A}(k_x,k_y)e^{-j(k_xx+k_yy+k_zz)}dk_xdk_y, \quad (1)$$

where $\overline{A}$ is a vector in the spectral domain. The integrand in (1) represents a plane wave traveling in the direction $k_x\hat{x}+k_y\hat{y}+k_z\hat{z}$ and since $\nabla\cdot\overline{E}=0$, it is noted that $\overline{A}.(k_x\hat{x}+k_y\hat{y}+k_z\hat{z})=0$. Substituting (1) into the wave equation, k_z is obtained as:

$$k_z=k_z^{\pm}=\pm\sqrt{k^2-k_x^2-k_y^2} \quad (2)$$

In (2), k is the wave number of the background medium in which the discrete scatterers of the random medium is included. Also, $k_z=k_z^+$ is for the waves that are traveling in $+\hat{z}$ direction, and $k_z=k_z^-$ is for the waves that are traveling in $-\hat{z}$ direction.

The tangential components of $\overline{A}$ (A_x and A_y) can be found by inverse Fourier transform (IFT) of the tangential components of $\overline{E}$ (E_x and E_y) at a constant plane $z=z_0$:

$$A_{x,y}(k_x,k_y)=e^{jk_zz_0}\int_{-\infty}^{+\infty}\int_{-\infty}^{+\infty}E_{x,y}(x,y,z_0)e^{j(k_xx+k_yy)}dxdy. \quad (3)$$

A_z component can be obtained from the other two components of $\overline{A}$:

$$A_z^{\pm}(k_x,k_y)=-\frac{k_xA_x+k_yA_y}{k_z^{\pm}}=-\frac{k_xA_x+k_yA_y}{\pm\sqrt{k^2-k_x^2-k_y^2}}. \quad (4)$$

In (4), A_z^+ is for the wave that is travelling in $+\hat{z}$ direction and A_z^- is for the wave that is travelling in $-\hat{z}$ direction.

Assuming a large but finite lateral dimensions for the slabs and periodic arrangement within xy-plane, discrete values for k_x and k_y must be used for plane waves in S-matrix method. In this case, discrete IFT can be applied to find $\overline{A}(k_x,k_y)$ for discrete values of k_x and k_y. In the S-matrix method only propagating waves with real k_z are included in the analyses and thus k_x and k_y must be sampled only in the circular region $k_x^2+k_y^2\le k^2$ (according to (2) for obtaining real values for k_z). To include all the propagating waves in the expansion, the spatial sampling interval (Δd) must be less than or equal to $\lambda/2$ (λ is the wavelength in the medium and is equal to $2\pi/k$). Since, in general, the spectrum of fields is not zero outside the region $k_x^2+k_y^2\le k^2$, aliasing in spectral domain may occur. To reduce aliasing, Δd must be chosen a value less than $\lambda/2$. However, smaller Δd requires larger computational resources and processing time. In this paper, Δd is selected to be $\lambda/4$. This value results in significant suppression of aliasing effect in the region $k_x^2+k_y^2\le k^2$ while does not require large computational resources. To further reduce the effect of aliasing, a window function can be applied to the fields before expansion to reduce high frequency spectral components.

According to the discrete Fourier transform properties, spacing of Δk between adjacent samples of k_x and k_y results in a periodic reconstructed field in spatial domain with period $2\pi/\Delta k$ along both x and y directions. In this paper, Δk is equal to $k/35$. This results in lateral dimensions of $35\lambda\times 35\lambda$ for uniquely calculating the fields from their spectral representation. With this spacing, total of 71×71 (=5041) samples are generated for k_x and k_y in the grid $-k\le k_x, k_y\le k$. Among them, 3841 samples are inside the visible region ($k_x^2+k_y^2\le k^2$) representing propagating waves. In the rest of the paper, N is the number of propagating plane waves in the wave spectral expansion.

A wave propagating in $+\hat{z}$-direction, which is called *Forward Propagating Wave*, is expanded by N plane waves with wave vector denoted by $\overline{k}_n^+$ $(=k_{x,n}\hat{x}+k_{y,n}\hat{y}+k_{z,n}^+\hat{z})$ for the nth ($n=1,2,\ldots,N$) plane wave. The superscript "+" indicates the quantity is related to the forward propagating wave. The forward propagating wave at z^- interface represents the incident wave on a slab with the corresponding electric field vector denoted by $\overline{A}_n^+$. The forward propagating wave at z^+ interface represents the wave exiting the slab with corresponding electric field vector denoted by $\overline{B}_n^+$.

The field propagating in $-\hat{z}$-direction, which is referred to as *Backward Propagating Wave*, is expanded by N plane waves with wave vector denoted by $\overline{k}_n^-$ $(=k_{x,n}\hat{x}+k_{y,n}\hat{y}+k_{z,n}^-\hat{z})$ for the nth ($n=1,2,\ldots,N$) plane wave. The superscript

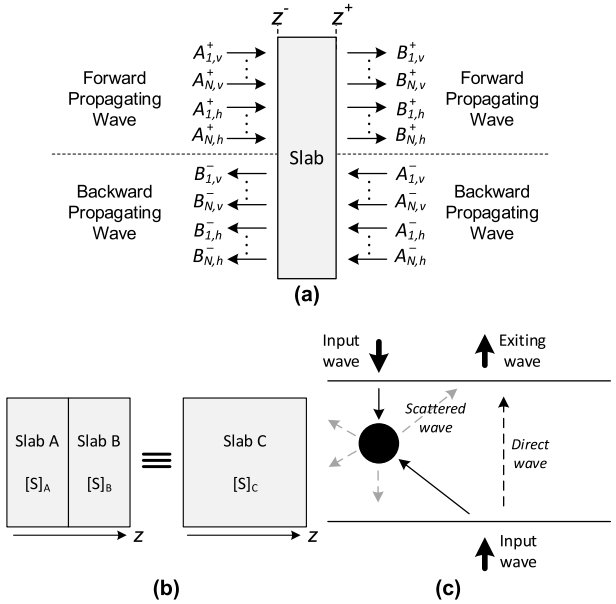

FIGURE 2. (a) Waves entering and exiting the slab. (b) Cascading the slabs. (c) direct and scattered waves in a slab.

"−" indicates the quantity is related to the backward propagating wave. The backward propagating wave at z^+ interface indicates an incident wave on slab and the corresponding electric field vector is denoted by $\overline{A_n^-}$. The backward propagating wave at z^- interface indicates a wave exiting from the slab and the corresponding electric field vector is denoted by $\overline{B_n^-}$.

To simplify the calculation of interaction of the plane waves with scatterers within a slab, it is convenient to decompose each plane wave into orthogonal vertical (v) and horizontal (h) polarized components. For this decomposition, the unit vectors for vertical polarization ($\widehat{v}$) and horizontal polarization ($\widehat{h}$) are defined by:

$$\begin{cases} \widehat{h}_n^{\pm} = \dfrac{\pm\widehat{z}\times\overline{k}_n^{\pm}}{\left|\pm\widehat{z}\times\overline{k}_n^{\pm}\right|} \\ \widehat{v}_n^{\pm} = \dfrac{\widehat{h}_n^{\pm}\times\overline{k}_n^{\pm}}{\left|\widehat{h}_n^{\pm}\times\overline{k}_n^{\pm}\right|} \end{cases}. \tag{5}$$

In (5), $\widehat{h}_n^+$ and $\widehat{v}_n^+$ are unit vectors for forward propagating waves and $\widehat{h}_n^-$ and $\widehat{v}_n^-$ are for backward propagating waves. The electric field for the nth plane wave is decomposed into vertical and horizontal polarizations as:

$$\begin{cases} \overline{A}_n^{\pm} = \left(\overline{A}_n^{\pm}\cdot\widehat{v}_n^{\pm}\right)\widehat{v}_n^{\pm} + \left(\overline{A}_n^{\pm}\cdot\widehat{h}_n^{\pm}\right)\widehat{h}_n^{\pm} \\ = A_{n,v}^{\pm}\widehat{v}_n^{\pm} + A_{n,h}^{\pm}\widehat{h}_n^{\pm} \\ \overline{B}_n^{\pm} = \left(\overline{B}_n^{\pm}\cdot\widehat{v}_n^{\pm}\right)\widehat{v}_n^{\pm} + \left(\overline{B}_n^{\pm}\cdot\widehat{h}_n^{\pm}\right)\widehat{h}_n^{\pm} \\ = B_{n,v}^{\pm}\widehat{v}_n^{\pm} + B_{n,h}^{\pm}\widehat{h}_n^{\pm}. \end{cases} \tag{6}$$

In (6), $A_{n,v}^{\pm}$, $A_{n,h}^{\pm}$, $B_{n,v}^{\pm}$, and $B_{n,h}^{\pm}$ are complex scalars. In this case, each of forward propagating wave and backward propagating wave is expanded by $2N$ plane waves at each of the two interfaces. For a fixed number of plane waves throughout the analyses, the wave vector and directions of vertical and horizontal unit vectors for nth plane wave is constant and as a result only the complex coefficients $A_{n,v}^{\pm}$, $A_{n,h}^{\pm}$, $B_{n,v}^{\pm}$, and $B_{n,h}^{\pm}$ in (6) are modified by propagation of waves and their interactions with scatterers.

In the S-matrix method, each slab is modeled as a network with $4N$ inputs and $4N$ outputs as illustrated in Fig. 2(a). In this case, the coefficients $A_{n,v}^{\pm}$, $A_{n,h}^{\pm}$, $B_{n,v}^{\pm}$, and $B_{n,h}^{\pm}$ are related by a $4N\times 4N$ matrix, S, as follows:

$$\begin{pmatrix} B_{1,v}^- \\ B_{2,v}^- \\ \vdots \\ B_{N,v}^- \\ B_{1,h}^- \\ B_{2,h}^- \\ \vdots \\ B_{N,h}^- \\ B_{1,v}^+ \\ B_{2,v}^+ \\ \vdots \\ B_{N,v}^+ \\ B_{1,h}^+ \\ B_{2,h}^+ \\ \vdots \\ B_{N,h}^+ \end{pmatrix} = \underbrace{\begin{pmatrix} [S_{11}] & [S_{12}] \\ [S_{21}] & [S_{22}] \end{pmatrix}}_{S} \begin{pmatrix} A_{1,v}^+ \\ A_{2,v}^+ \\ \vdots \\ A_{N,v}^+ \\ A_{1,h}^+ \\ A_{2,h}^+ \\ \vdots \\ A_{N,h}^+ \\ A_{1,v}^- \\ A_{2,v}^- \\ \vdots \\ A_{N,v}^- \\ A_{1,h}^- \\ A_{2,h}^- \\ \vdots \\ A_{N,h}^- \end{pmatrix}. \tag{7}$$

Similar to the network theory, if the z^- interface is considered as port 1 and z^+ interface is considered as port 2, in (7):

- the $2N\times 2N$ matrix $[S_{11}]$ relates the waves exiting the slab at z^- interface to the waves entering the slab at z^- interface,
- the $2N\times 2N$ matrix $[S_{21}]$ relates the waves exiting the slab at z^+ interface to the waves entering the slab at z^- interface,
- the $2N\times 2N$ matrix $[S_{12}]$ relates the waves exiting the slab at z^- interface to the waves entering the slab at z^+ interface, and
- the $2N\times 2N$ matrix $[S_{22}]$ relates the waves exiting the slab at z^+ interface to the waves entering the slab at z^+ interface.

In the next section the elements of S matrix is derived for a slab.

In the field expansion in (1), the z-position of the origin of the coordinate system is not important. Assuming that the fields are known at $z = z_0$ (source plane), the fields at $z = z_0 + z_d$ (observation plane) are obtained by using (1) and (3) as:

$$\begin{aligned} &E_{x,y}(x, y, z_0 + z_d) \\ &= \frac{1}{4\pi^2}\int_{-\infty}^{+\infty}\int_{-\infty}^{+\infty}\left(e^{jk_z z_0}\int_{-\infty}^{+\infty}\int_{-\infty}^{+\infty}E_{x,y}(x', y', z_0)e^{j(k_x x' + k_y y')}dx'dy'\right) \\ &\times e^{-j(k_x x + k_y y)}e^{-jk_z(z_0+z_d)}dk_x dk_y. \end{aligned} \tag{8}$$

In (8), the terms including z_0 are cancelled out and the term including z_d ($e^{-jk_z z_d}$) remains. The same is true for z-component of the field. This shows that the evaluation of fields does not depend on the choice of the z-position for the origin of coordinate system, and it only depends on the difference between the z-positions of the source plane and the observation plane, i.e., z_d. The term $e^{-jk_z z_d}$ shows the propagation of planes waves in $+\widehat{z}$ or $-\widehat{z}$ direction (depending on k_z) from the source plane to the observation plane. This term is included in the elements of S matrix as discussed in the next section.

If plane wave coefficients are known for v and h polarizations, denoted by $C_{n,v}$ and $C_{n,h}$, respectively, at a plane, the corresponding total field at the same plane can be calculated from:

$$\overline{E}(x,y) = \sum_{1}^{N} \left(C_{n,v}\widehat{v}_n + C_{n,v}\widehat{h}_n\right) e^{-j\left(k_{x,n}x + k_{y,n}y\right)}. \tag{9}$$

As an example, if the wave exiting the slab is calculated at z^+ interface, then $C_{n,v}$, $C_{n,h}$, $\widehat{v}_n$, and $\widehat{h}_n$ in (9) are $B^+_{n,v}$, $B^+_{n,h}$, $\widehat{v}^+_n$, and $\widehat{h}^+_n$, respectively.

If the S-matrices are known for slab A and slab B (S_A and S_B, respectively), then the equivalent S-matrix for the cascaded slab C in Fig. 2(b), S_C, can be obtained by the formulas presented in [24] for general multi-port networks. The submatrices in (7) for S_c are related to those of S_A and S_B by:

$$\begin{cases} [S_{C,11}] = [S_{A,11}] + [S_{A,12}][S_{B,11}](I - [S_{A,22}][S_{B,11}])^{-1}[S_{A,21}] \\ [S_{C,21}] = [S_{B,21}](I - [S_{A,22}][S_{B,11}])^{-1}[S_{A,21}] \\ [S_{C,12}] = [S_{A,12}][S_{B,12}] + [S_{A,12}][S_{B,11}](I - [S_{A,22}][S_{B,11}])^{-1}[S_{A,22}][S_{B,12}] \\ [S_{C,22}] = [S_{B,22}] + [S_{B,21}](I - [S_{A,22}][S_{B,11}])^{-1}[S_{A,22}][S_{B,12}]. \end{cases} \tag{10}$$

Here, I is a $2N\times\ 2N$ identity matrix.

To analyze a random medium, first, the S-matrices for all slabs are calculated separately and then the overall S-matrix is obtained by cascading all slabs using (10). Then the fields due to a source (or multiple sources) are evaluated and expanded as incoming waves to form the vector on the right-hand-side of (7), i.e., the *source vector*. If the source is close to the z^- interface of the first slab, then the electric field of source is evaluated and expanded at z^- interface as incoming wave. The resulting wave coefficients form $A^+_{n,v}$ and $A^+_{n,h}$ ($n = 1, 2, \ldots, N$) in the source vector in (7) and $A^-_{n,v}$ and $A^-_{n,h}$ for this source are zero. If the source is close to the z^+ interface of the last slab, then the electric field of source is evaluated and expanded at z^+ interface as incoming wave. The resulting wave coefficients form $A^-_{n,v}$ and $A^-_{n,h}$ in the source vector in (7) and $A^+_{n,v}$ and $A^+_{n,h}$ for this source are zero. If multiple sources are present, the same coefficients in the source vector are added. By multiplying the source vector by the S-matrix in (7), the left-hand-side vector is obtained. Using the last $2N$ elements of this vector in (9) results the total electric field for the wave exiting the last slab. On the other hand, using the first $2N$ elements results the total electric field for the wave exiting the first slab.

III. ELEMENTS OF THE S-MATRIX FOR A SLAB CONTAINING SCATTERERS

The wave exiting a slab at an interface can be decomposed into waves entered the slab at the other interface and directly propagated to the output, which is referred to as the *direct wave*, and waves entered the slab from both interfaces and scattered by the scatterers, which is referred to as the *scattered waves*. This is illustrated in Fig. 2(c).

The contribution of the direct wave is represented by the S-matrix S_{direct} and that of the scattered waves is denoted by the S-matrix $S_{scattered}$. The S-matrix of the slab is equal to $S_{direct} + S_{scattered}$.

The method described in Section II is accurate if the lateral extent of the slabs is large. The accuracy degrades when the propagation distance (the length of the cascaded slabs) becomes large. This mainly affect the mean-field component of the propagating wave. To circumvent this difficulty and enhance the accuracy of field computation with moderate size of the lateral dimensions of the slabs, a correction approach is also developed.

A. CALCULATION OF THE DIRECT WAVE USING GREEN'S FUNCTION

To calculate the direct wave at the output plane, Green's function in conjunction with the field equivalence theorem and image theory are used. In this method, first, for each plane wave entering the slab, the electric field ($\overline{E}(x,y)$) is calculated at the input interface over the region $-\frac{\pi}{\Delta k} \le x, y \le \pi/\Delta k$ (extent of the slab) using (9). Assuming the fields are zero in the region outside the extent of the slab, using the equivalence theorem and image theory, the equivalent magnetic currents can be calculated as:

$$\overline{j}^n_m = -2\widehat{n} \times \overline{E}_n(x,y), \tag{11}$$

where $\widehat{n}$ is $+\widehat{z}$ for forward propagating waves and $-\widehat{z}$ for backward propagating waves. Using the tangential components of the magnetic current ($J_{m,y}$ and $J_{m,x}$), the tangential components of the electric field can be calculated at the output interface using the free-space Green's function as:

$$\begin{cases} E^n_x(\overline{r}) = -\frac{k^2}{4\pi}\int_{-\frac{\pi}{\Delta k}}^{\frac{\pi}{\Delta k}}\int_{-\frac{\pi}{\Delta k}}^{\frac{\pi}{\Delta k}} \left(j + \frac{1}{k|\overline{r}-\overline{r}'|}\right)\frac{e^{-jk|\overline{r}-\overline{r}'|}}{k|\overline{r}-\overline{r}'|} \\ J^n_{m,y}(x',y') \times \frac{(\overline{r}-\overline{r}').\widehat{z}}{|\overline{r}-\overline{r}'|}dxdy \\ E^n_y(\overline{r}) = +\frac{k^2}{4\pi}\int_{-\frac{\pi}{\Delta k}}^{\frac{\pi}{\Delta k}}\int_{-\frac{\pi}{\Delta k}}^{\frac{\pi}{\Delta k}} \left(j + \frac{1}{k|\overline{r}-\overline{r}'|}\right)\frac{e^{-jk|\overline{r}-\overline{r}'|}}{k|\overline{r}-\overline{r}'|} \\ J^n_{m,x}(x',y') \times \frac{(\overline{r}-\overline{r}').\widehat{z}}{|\overline{r}-\overline{r}'|}dx'dy'. \end{cases} \tag{12}$$

In (12), $\overline{r}$ is the position vector on the output plane with the origin at the center of the input plane and is equal to $x\widehat{x}+y\widehat{y}+d_s\widehat{z}$ for forward propagating waves and $x\widehat{x}+y\widehat{y}-d_s\widehat{z}$ for backward propagating waves. $\overline{r}' = x'\widehat{x}+y'\widehat{y}$ is the position vector on the input plane.

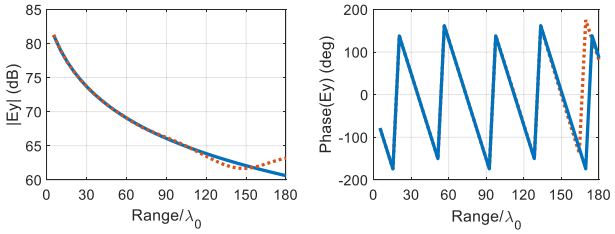

FIGURE 3. E_y of a y-directed Hertzian dipole at different distances from the dipole, (a) amplitude and (b) phase (solid line: actual values, dotted line: S-matrix and Green's function method).

The tangential fields at the output plane obtained from (12) are expanded in terms of plane waves to find the wave coefficients for the exiting wave from the slab (B coefficients). In this method, each input plane wave at an interface, affects all plane waves exiting at the other interface and therefore, all elements in $S_{direct,21}$ and $S_{direct,12}$ are non-zero. $S_{direct,11}$ and $S_{direct,22}$ are zero matrices.

The power density of a plane wave exiting a slab is lower than its value at the input since a part of its power is coupled to another plane waves indicated by the non-zero non-diagonal elements of $S_{direct,21}$ and $S_{direct,12}$. This introduces some error in the fields as the waves propagate. Using larger periods will result in smaller non-diagonal components and less error for a given range. Figure 3 shows amplitude and phase of the electric field (E_y) of a y-directed Hertzian dipole propagating along z-direction as a function of range using the exact solution and the Green's function/S-matrix method. The dipole is 50 mm away from the first slab. The thickness of each slab (d_s) is $5.13\lambda_0$. The lateral dimension of slab is $35\lambda_0 \times 35\lambda_0$. It can be observed that the calculated fields using Green's function and S-matrix method are accurate up to a range of about $120\lambda_0$.

To resolve the issue with the limited range of validity for the Green's function method, a correction scheme is introduced in Appendix A. In this method, the random medium is divided into *super slabs* with a length slightly smaller than the range of validity of the Green's function method (about $120\lambda_0$ for the example considered here). Then the analysis is pursued with cascaded super slabs and the correction algorithm enforced. In this approach the fluctuation and mean part of the fields entering each super slab are first estimated and separated and then the mean field component is replaced by a mean field directly calculated using the effective medium index of refraction (similar to Foldy's method [17]) obtained from the previous step. With this correction the accumulation of error in the mean field as the waves travel in the random medium is avoided.

B. THE SCATTERED WAVE CALCULATION

A slab, depending on the concentration of particles, may contain one or more scatterers. To include the effect of scattering in the S-matrix of the slab ($S_{scattered}$), the following steps are followed:

1) A local coordinate system is defined for the slab with the origin at the center of the input plane.

2) For each input plane wave, the phase term modeling the propagation of the plane wave from the origin of the local coordinate to the center of the scatterer is calculated. Assuming that the center of the scatterer is at (x_c, y_c, z_c) in the local coordinate system, for the nth plane wave this term is:

$$P_n = e^{-jk_{x,n}x_c} e^{-jk_{x,n}y_c} e^{-jk_{z,n}z_c}. \tag{13}$$

3) Assuming the response of the scatterer to any input plane wave is known, the scattered fields due to the scatterer is calculated at the input and output planes considering its location.

4) The scattered fields at the input and output planes are expanded and the resulting coefficients are added to $S_{scattered}$.

5) Steps 1 to 4 are repeated for all input plane waves (at both interfaces) and also for all scatterers in the slab.

In this paper, for simplicity, the scatterers are assumed to be lossy dielectric spheres which have analytical solution for the scattering due to the incident plane wave (Appendix B).

IV. SIMULATION RESULTS

In this section, the S-matrix method is employed for calculation of wave propagation and scattering through rain for different rain rates and within different frequencies at mm-wave band. The simulated specific attenuation is compared to the measured values/models for rain reported in the literature.

A. STATISTICAL CHARACTERISTICS OF RAIN

Rain as a random medium is defined by *drop size distribution (DSD)*. DSD which is denoted by $\widetilde{N}(D)$ is used to find the total number of rain droplets per unit volume (N_D):

$$N_D = \int_{D_1}^{D_2} \widetilde{N}(D)\mathrm{d}D. \tag{14}$$

In (14), for $\widetilde{N}(D)$ with the unit ($\mathrm{m}^{-3}\mathrm{cm}^{-1}$), N_D is the total number of rain droplets with diameters (in cm) between D_1 and D_2 per 1 m^3.

$\widetilde{N}(D)$ has been parametrized by exponential [15], log-normal, or gamma distribution [16]. Among them, gamma distribution can accurately model wide range of naturally occurring DSDs [25]. DSD based on gamma distribution is represented by [16]:

$$\widetilde{N}(D) = N_0 D^{\mu} e^{-\Lambda D}, \qquad 0 \le D \le D_{\max}, \tag{15}$$

where D (in cm) is the diameter of a sphere with the same volume as a rain droplet. μ is the distribution parameter and can be a negative, positive, or zero. N_0 is a coefficient with the unit ($\mathrm{m}^{-3}\mathrm{cm}^{-1-\mu}$). Λ has the unit (cm^{-1}) and is described by [16]:

$$\Lambda = \frac{3.67 + \mu}{D_0}. \tag{16}$$

TABLE 1. Rain gamma distribution parameters for different rain rates.

Rain Rate	Description	D_0	μ	N_0
2 mm/hr	Drizzle (light rain)	0.095	0.18	1.96×10^5
5 mm/hr	Moderate rain	0.115	0.18	1.96×10^5
10 mm/hr	Shower (heavy rain)	0.186	0.18	1.96×10^5
25 mm/hr	Shower (heavy rain)	0.177	1.63	7.54×10^6
50 mm/hr	Thunderstorm	0.25	1.9	7.54×10^6

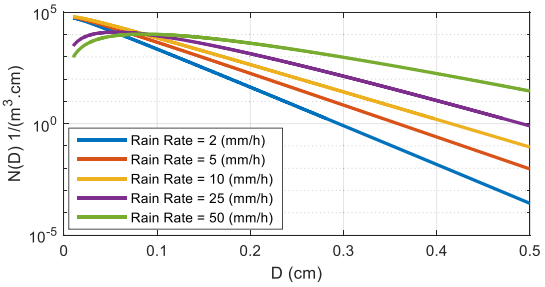

FIGURE 4. DSD for the rain types in Table 1.

TABLE 2. Number of particles per unit volume for different particle diameter ranges at different rain rates.

Particle Diameter (cm)	Diameter Range in DSD (cm)	N_D (m^{-3})				
		R 2 mm/hr	R 5 mm/hr	R 10 mm/hr	R 25 mm/hr	R 50 mm/hr
0.015	0.01–0.02	505	560	600	51	21
0.03	0.02–0.04	630	770	883	200	100
0.05	0.04–0.06	308	435	545	255	170
0.07	0.06–0.08	145	237	325	244	200
0.1	0.08–1.05	116	241	385	512	650
0.2	0.15–0.5	8	29	65	183	558

Here D_0 is the median diameter in (cm) and is a function of the rain rate, R.

In this paper, five different rate rates are considered for simulations and their distribution parameters are summarized in Table 1 [25] and their DSDs are plotted in Fig. 4.

In S-matrix method, to speed up the calculations, the scattered fields of a particle due to different input plane waves are precalculated and stored and used when the S-matrix for any slab containing such particles are calculated. Since the scattered fields cannot be stored for large number of particle types, a limited number of particles with different diameters are selected. For this purpose, six different diameters are considered for spherical rain particles which are listed in Table 2. In Table 2, for all selected rain rates, each selected diameter is approximately the mean diameter within the indicated range in the second column. For a rain rate, N_D for each rain droplet type is obtained by integrating the $\widetilde{N}(D)$ of that rain rate in the indicated range in the second column of Table 2. N_Ds in Table 2 are used to generate the random media for simulations.

B. RAIN DROPLET DIELECTRIC CONSTANT

The most accurate model for complex dielectric constant of water is *double-Debye dielectric model (D3M)* which is valid up to 1000 GHz [26]. The complex dielectric constant of pure water versus frequency at 20°C is derived using D3M and shown in Fig. 5. These values are used for simulations.

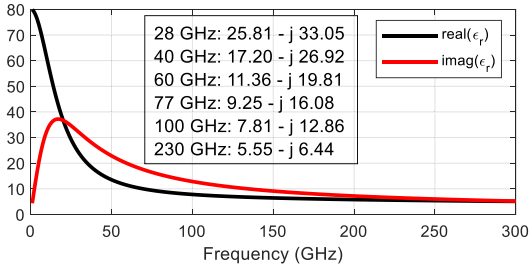

FIGURE 5. Complex dielectric constant of rain droplets (pure water) at 20°C.

C. SIMULATION PARAMETERS

For simulations in this paper, the lateral dimensions for the slabs are chosen to be $35\lambda_0\times\ 35\lambda_0$ where λ_0 is the free-space wavelength at the frequency of simulation. The selected frequencies are 28, 40, 60, 77, 100, and 230 GHz. As mentioned in Section II, the spacing for field samples in spatial domain is selected to be $\lambda_0/4$ and a raised cosine window is applied to the fields before expansion. The spacing between samples of k_x and k_y (Δk) is selected to be $k_0/35$. In this case, N is 3841.

In S-matrix method presented here the multiple scattering within a slab is not considered, and thus the maximum number of particles per slab must be limited by properly selecting the slab thickness. With the specified particle distributions in Table 2 and lateral dimension for slabs, the slab thickness is selected to be 0.02 m in the simulations. With this thickness, in the generated random media based on the specified distributions, the number of scatterers within each slab never exceeds 3. This is important in the accuracy of the S-matrix method as it does not consider multiple scattering between scatterers within a given slab. For very dense random media with strong scatterers, the thickness of each slab must be decreased to limit the maximum number of scatterers per slab.

For simulation at 28, 40, 60, and 77 GHz, the number of slabs in each super slab is chosen to be 20 resulting in a total thickness of 0.4 m for the super slab. In this case the largest super slab thickness in terms of λ_0 is $103\lambda_0$ (at 100 GHz) which is below the range of validity $120\lambda_0$ shown in Fig. 3. At 100 GHz and 230 GHz, the number of slabs per super slab is 15 (super slab length is $100\lambda_0$) and 7 (super slab length is $107\lambda_0$), respectively.

A y-polarized electric field distribution (spherical wavefront) with farfield 3-dB beamwidth of 1.65° is placed at the z^- interface of the first slab of the first super slab.

All the rain particles in the simulation are considered to be spheres with dielectric constants indicated in Fig. 5 and diameters listed in the first column of Table 2. For each rain type, five different random media with length of 400 m and particle distribution following Table 2 are generated to perform Monte Carlo simulations.

D. SIMULATION VALIDATION

In this section, the accuracy of S-matrix method in a scenario involving a few numbers of scatterers is investigated

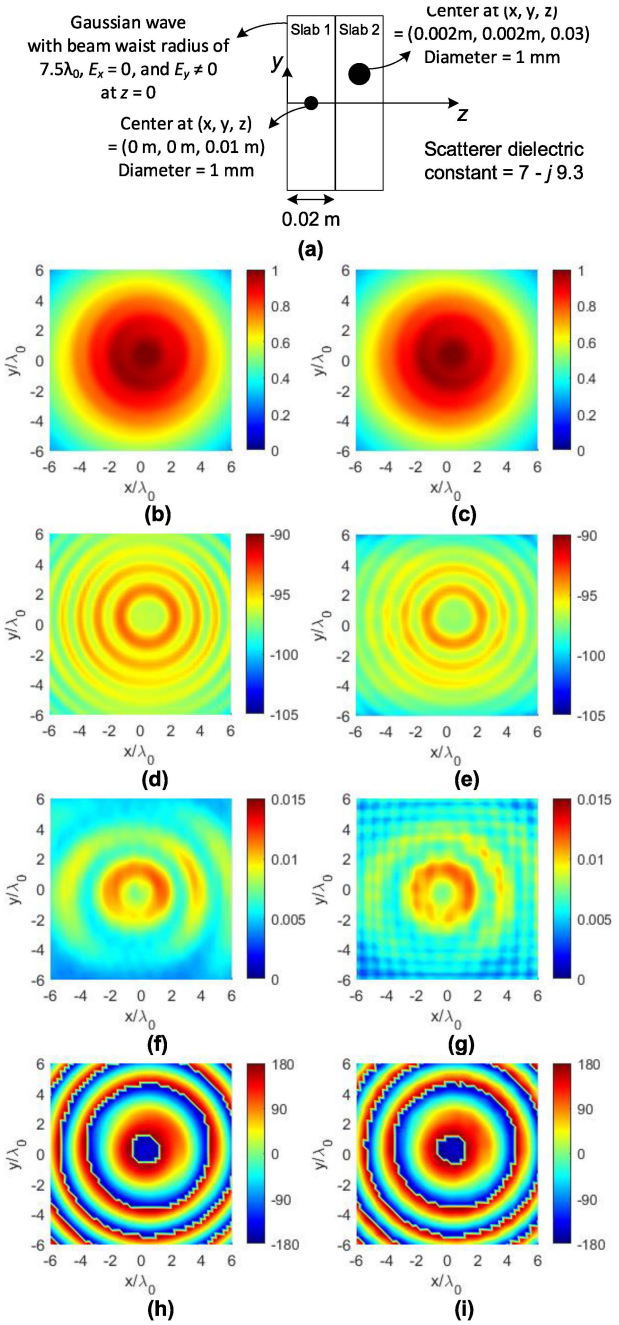

FIGURE 6. Validation of the S-matrix method. (a) Geometry of the problem. Amplitude of E_y (in dB) at z^+ interface of the second slab ($z = 0.04$ m): (b) S-matrix method and (c) COMSOL. Phase of E_y (in deg) at z^+ interface of the second slab: (d) S-matrix method and (e) COMSOL. Amplitude of E_y (in dB) at z^- interface of the first slab ($z = 0$ m): (f) S-matrix method and (g) COMSOL. Phase of E_y (in deg) at z^- interface of the first slab: (h) S-matrix method and (i) COMSOL.

using COMSOL 3-D full-wave simulations. Since the lateral dimension of slabs is large compared to the wavelength, only a few numbers of cascaded slabs can be simulated by COMSOL. Figure 6(a) shows the geometry of the problem which includes two cascaded slabs. One spherical particle is present within each slab. The diameter, complex dielectric constant, and location of the center of particles are mentioned in Fig. 6(a). The simulation parameters for S-matrix method are the same as those in Section IV-C and the simulation frequency is 77 GHz. Assuming the input wave at the bottom of the first slab is a Gaussian beam with beam waist radius of $7.5\lambda_0$ and $E_y \neq 0$ and $E_x = 0$ at $z = 0$, the amplitude and phase of forward propagating E_y at z^+ interface of the second slab is shown for S-matrix method in Fig. 6(b) and 6(d) and for COMSOL in Fig. 6(c) and 6(e), respectively. The amplitude and phase of backward propagating E_y (due to scattering by the particles) at z^- interface of the first slab is shown for S-matrix method in Fig. 6(f) and 6(h) and for COMSOL in Fig. 6(g) and 6(i), respectively. The results confirm the accuracy of S-matrix method in analyses of large problems including sparse scatterers.

E. SIMULATION RESULTS FOR WAVE PROPAGATION IN RAIN

In this section, S-matrix simulation results for wave propagation through rain at different frequencies within the mm-wave band are presented. The simulation parameters are described in Section IV-C.

In the simulations, after correction of the electric fields at the output of a super slab, the electric field is calculated on the z^+ interface of that super slab and the total power of the y- component of the field, P_{Ey}, is calculated by integrating $|E_y|^2/\eta_0$ over the slab interface where η_0 is the free-space wave impedance. Because of multiple scattering among particles within a random medium, the electric field phase and amplitude fluctuations increase as r increases. This is shown in Fig. 7(a) and (b) at 77 GHz for rain rate 50 mm/hr. As an example, Fig. 7(c) shows that the phase fluctuation increases as the range increases from 20 m to 75 and 150 m. Fig. 7 also shows the ability of the S-matrix method in capturing the phase and amplitude variation of the waves propagating in the random medium.

At far distances from the source (r), considering only free space path loss, the power decreases by $1/r^2$. In this case, multiplying P_{Ey} by r^2 must remove the effect of free-space path loss and the resulting quantity must remain constant over range. However, in the presence of rain, the quantity $P_{Ey} \times r^2$ is reduced with r. The rate of this reduction indicates the attention of waves by the rain medium. Figure 8 shows P_{Ey} and $P_{Ey} \times r^2$ versus r for rain rates 2 mm/hr and 50 mm/hr at 77 GHz (the random medium is generated using the particle distribution in Table 2). The slope of the dashed line in Fig. 8 which is fitted to $P_{Ey} \times r^2$ at ranges less than 100 m, shows the attenuation by rain. The fluctuations in phase and amplitude of fields at high ranges (as shown in Fig. 7) result in fluctuations in the power shown in Fig. 8(b). After a certain range, which is called the *knee point* in [23], the fluctuating part of fields dominates the mean component, resulting in a lower specific attenuation compared to the near ranges. This is shown in Fig. 8(b) where moving average of power over ranges of 30 m is shown by a dotted line. It can be observed that after 150 m (the knee point), the dotted line deviates from the dashed line (which means a lower specific attenuation after the knee point). It is noted

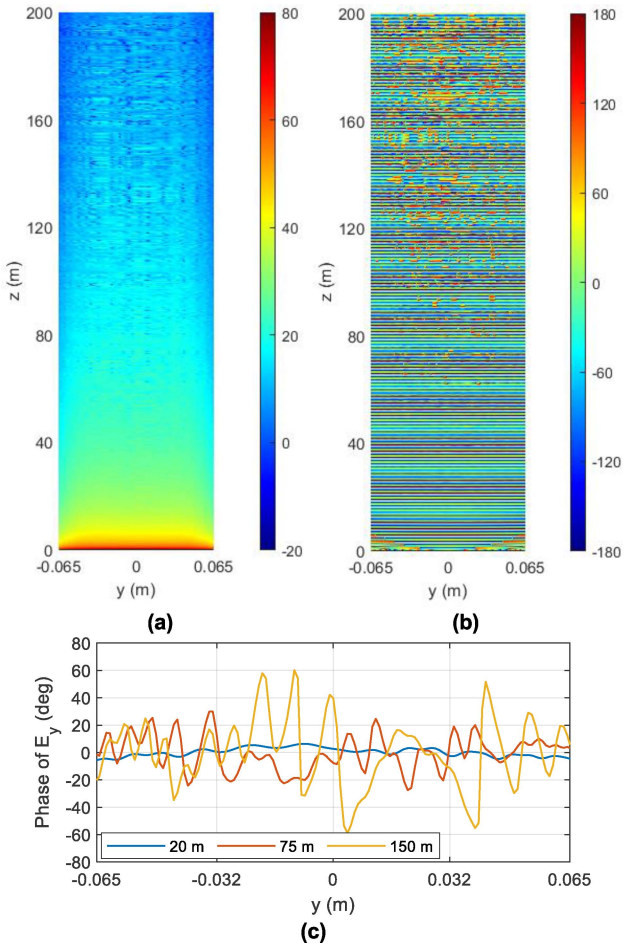

FIGURE 7. (a) amplitude (in dB) and (b) phase (in deg) in yz-plane and (c) phase (in yz-plane) at different ranges for the forward propagating electric field (E_y) in rain (50 mm/hr) at the outputs of super slabs at 77 GHz.

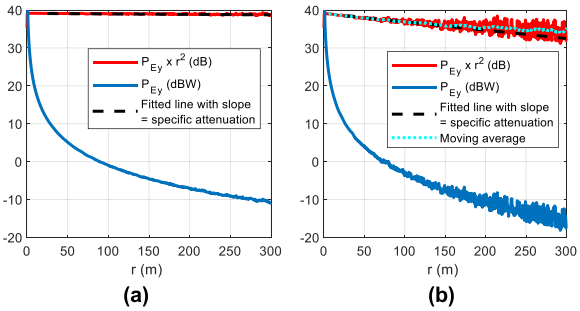

FIGURE 8. Power of E_y at the outputs of super slabs at different distances from the source (r) at 77 GHz for rain rate (a) 2 mm/hr and (b) 50 mm/hr. Slope of the dashed line is the specific attenuation in dB/m.

that at lower rain rates where the scattering is lower, the knee point occurs at larger ranges.

The specific attenuation (before the knee point) for different rain rates at different frequencies obtained by S-matrix method and Monte Carlo simulations is summarized in Table 3. The attenuation predicted by Foldy's method considering single scattering assumption is also included in Table 3. It can be observed that in all cases Foldy's method overestimates the rain specific attenuation.

TABLE 3. Specific attenuation in dB/km (before the knee point) for different rain rates at different frequencies (S-matrix/Foldy's method).

Freq. / Rate	28 (GHz)	40 (GHz)	60 (GHz)	77 (GHz)	100 (GHz)	230 (GHz)
2 mm/hr	0.2751/ 0.2844	0.4719/ 0.6224	0.7183/ 1.2025	1.2318/ 1.8398	2.1605/ 2.4820	2.8354/ 3.4052
5 mm/hr	0.7417/ 0.7918	0.9456/ 1.6875	1.6548/ 2.8736	2.4380/ 4.0716	4.0908/ 5.1946	4.9601/ 6.3009
10 mm/hr	1.3750/ 1.5853	1.8637/ 3.3294	2.5006/ 5.2555	4.0390/ 7.0600	5.0097/ 8.6900	7.4094/ 9.8390
25 mm/hr	3.1090/ 3.7984	6.1877/ 7.7798	7.7183/ 10.6207	10.8705/ 12.6136	10.9198/ 14.2376	9.5397/ 13.7045
50 mm/hr	8.2750/ 10.6905	16.0551/ 21.5663	22.2030/ 26.7240	24.5244/ 28.7097	25.1860/ 30.5218	20.1818/ 28.0093

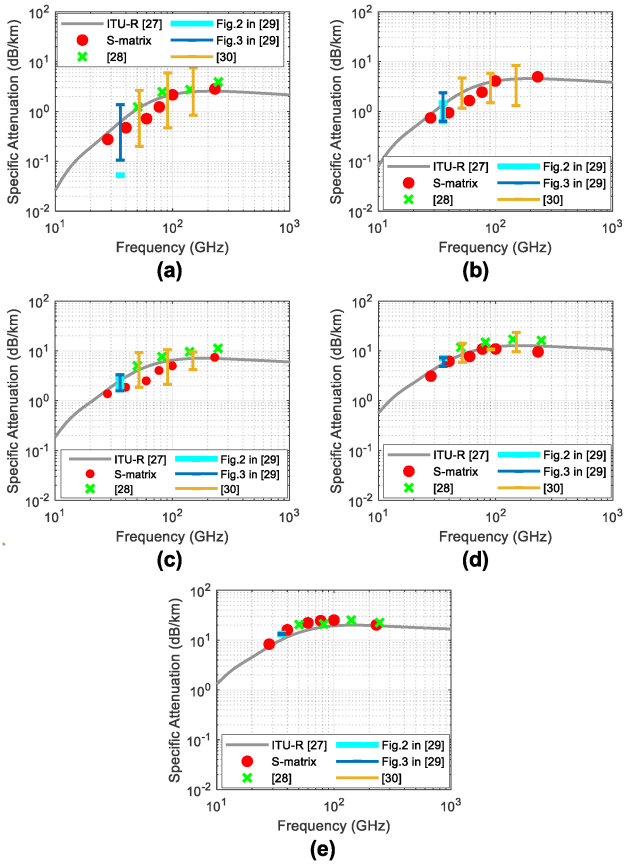

FIGURE 9. Comparison of the specific attenuation predicted by the S-matrix method with the ITU-R P836-3 model [27] and the measured results in [28], [29], [30] for rain rate (a) 2 mm/hr, (b) 5 mm/hr, (c) 10 mm/hr, (d) 25 mm/hr, and (e) 50 mm/hr.

Figure 9 shows the calculated specific attenuation over frequency for different rate rates. Figure 9 also shows the ITU-R P836-3 model [27] and the measured data in [28], [29], [30]. At the lower rain rates (2, 5, and 10 mm/hr), the measured specific attenuation has a wide variation range which indicates that the specific attenuation is highly sensitive to the particle distribution at low rain rates. Since the particle distribution for ITU-R model is not specified, the specific attenuations calculated by S-matrix (based on the selected particle distribution in Table 2) deviate from ITU-R model, but the results still fall within the range of the variation of the measured results. At high rain rates (25 and 50 mm/hr) where the range of variation of

specific attenuation at each frequency reduces in measurement results, ITU-R model and measured results as well as the S-matrix method predict almost the same specific attenuation values.

Table 4 compares the measured specific attenuation for different rain rates and frequencies and the simulation results by S-matrix method with ITU-R P836-3 model. In majority of cases, the measured values show a larger variation range than the range predicted by ITU-R model. Even for a fixed rain rate, the reported measured specific attenuation has a relatively large range of variations which can be attributed to different rain particle distributions for a given rain rate. The S-matrix method results with rain particle distribution in Table 2 fall within the range of measured results. A comprehensive list of measured results is provided in [13].

V. CONCLUSION

A method for accurate analyses of scattering and propagation through random media is presented. In this method, the random medium is divided into finite-size slabs and each slab containing a few numbers of scatterers is modeled as a network with multiple input/output ports described by a S-matrix. The entire random medium is modeled by cascading the S-matrices. Unlike available methods, the proposed method considers multiple scattering between the scatterers and therefore it can be applied in analyses of both strong and weak scatterers with any shape. The method tracks the polarization and phase information of waves along the path of propagation. Hence it can provide the phase front aberration and depolarization of the waves propagating through the random medium. This is a useful information in performance assessment of coherent imaging radars and communication systems.

APPENDIX A
CORRECTION SCHEME FOR THE S-MATRIX METHOD

As mentioned earlier, for estimation of the mean field (coherent component) over long distance propagation, the lateral dimension of the slab must be very large. But that will make the computation very inefficient. In this Appendix, a correction scheme to the S-matrix is described for forward propagating wave. Total forward propagating electric field at an observation point is composed of three components: 1) the incident electric field due to direct propagation of waves from source to the observation point without any interaction with scatterers, 2) the mean scattered electric field, and 3) the fluctuating part of the scattered field. In a sparse random medium, the summation of incident and mean scattered waves can be obtained by modeling the random medium as a homogeneous medium with an effective complex refractive index, n_{eff}, providing the same attenuation (before the knee point) for the waves.

The correction scheme is illustrated in Fig. 10 for forward propagating waves (the same procedure can be followed in the reverse direction for the backward propagating waves). Because of the limited range of validity of Green's function method, instead of cascading S-matrices of all slabs in the random medium, the random medium is divided into *super slabs* with maximum length of L and only the slabs belonging to the same super slab are cascaded as depicted in Fig. 10(a). The length L is selected a value less than the maximum range of validity of the Green's function method (with the S-matrix method parameters described in the last sections and according to Fig. 3, L is $120\lambda_0$).

The correction scheme works as follows. At the z^- interface of the nth super slab, the total corrected electric field from the last super slab ($E^{t,\ corrected}_{(n-1)}$) is expanded and used as a source in (7). As shown in the Fig. 10(a), the components of the resulting total forward propagating wave at the output of the nth super slab (E^t_n) are:

1) E^i_n: the incident electric field propagating in free space from the source (Fig. 10(a)) to the z^+ interface of nth super slab without any interaction with scatterers.
2) $<E^s_n>$: the mean scattered field due to the input wave that passed through the nth super slab without interacting with scatterers.
3) $<E^{s,c}_n>$: the mean scattered wave due to the interaction of the input wave by the scatterers within the nth super slab.
4) $\widetilde{E}^s_n$: the fluctuating part of the scattered wave due to the input wave that passed through the nth super slab without interacting with scatterers.
5) $\widetilde{E}^{s,c}_n$: the fluctuating part of the scattered field due to the interaction of the input wave by scatterers within the nth super slab.
6) $\widetilde{E}^{s,m}_{n,n+1}$: the scattered field due to multiple scattering between super slabs n and $(n+1)$.

Each of the first five components in the output wave (E^t_n) have a level of error which will be accumulated if it is not corrected. To do the correction, the fifth component, $\widetilde{E}^{s,c}_n$, must be estimated and separated from the other components. As depicted in Fig. 10(b), the summation of the first five components, E^b_n, can be obtained by calculating the forward propagating wave at the z^+ interface of the nth super slab using the same source as Fig. 10(a) and S-matrix of the nth super slab ($[S_n]$). As depicted in Fig. 10(c), the summation of the first four components (E^c_n) can be obtained by calculating the forward propagating wave at the z^+ interface of the nth super slab due to the same source as Fig. 10(a) while the super slab with random particles is replaced by a super slab with the same lateral dimension and thickness but filled with a homogeneous material with refractive index of n_{eff}. As shown in Fig. 10(c), for this calculation, S' is the S-matrix of the substitute super slab and E^c_n is the total output field. In this case, $\widetilde{E}^{s,c}_n = E^b_n - E^c_n$.

As depicted in Fig. 10(d), at ranges close to the source where the region within the beamwidth of the source is

TABLE 4. Comparison of the measured rain specific attenuation for terrestrial links and simulation results by S-matrix method with ITU-R P836-3 model.

Ref.	Description	Polarization	Frequency (GHz)	Range (km)	Rain rate (mm/hr)	Specific attenuation (dB/km)	ITR-R model* (dB/km)
[28]	Measured 20 m above the ground	Horizontal	50.4	0.81	2–90	1–30	1.2–25.2
			81.8			2–30	1.9–28.8
			140.7			2–30	2.5–29.5
			245.5			3–30	2.5–28.4
[29]	Measured	Vertical	38.5	0.448	5–50	0.05–13.5	1.6–11
					2–55	0.1–13	0.7–12
[30]	Measured 60 m above the ground	Vertical	52	1.008	0.2–25	0.2–14	0.2–8.4
			90.9			0.2–10.5	0.4–11.7
			150			0.2–23	0.6–12.7
[31]	Measured	Right-handed circular	11.5	1.3	90	3.2	4
			34.5			14.7	17.9
		Horizontal	81.8			25.8	28.8
[14]	Measured	Vertical	38	3.2	10.58	3.3	2.9
					49.79	20.89	15.6
					98.57	30.8	19.5
[32]	Measured	Vertical	120	0.4	20	6.3–12.5	10.8
					40	6.3–20	17.1
					60	18.8–25	22.3
This work	Simulated using S-matrix method**	Vertical	28	0.4	2–50	0.3–8.3	0.4–7.4
			40			0.5–16	0.8–11.5
			60			0.7–22.2	1.4–15.9
			77			1.2–24.5	1.8–17.9
			100			2.2–25.2	2.2–19.3
			230			2.8–20.2	2.6–19.4

*At the same frequency, rain rate range, and polarization
**Based on distribution in Table 2 and before the knee point. The values are also listed in detail in Table 3.

smaller than the slab extent, $\widetilde{E}_n^{s,c}$ is correct. However, at far ranges, where slab extent is smaller than area within the beamwidth, $\widetilde{E}_n^{s,c}$ is underestimated and must be corrected. As illustrated in Fig. 10(d), at far ranges, the scatterers outside the slab extent will contribute to the scattered field within the slab, but these scatters are not included in S-matrix method. Noting that the fluctuating part of scattered fields due to scatters are not coherent, the power of scattered fields due to scatterers outside the slab must be added to the scattered fields due to scatterers within the slab. To correct for $\widetilde{E}_n^{s,c}$, a factor of $\sqrt{A'(R)/A}$ is used, that is:

$$\widetilde{E}_n^{s,c,corrected} = \begin{cases} \widetilde{E}_n^{s,c}, & A > A'(R) \\ \widetilde{E}_n^{s,c} \times \sqrt{A'(R)/A}, & A < A'(R) \end{cases}, \quad (17)$$

where A is the area of the slab interface and $A'(R)$ is the area within the beamwidth of the source at the range R (Fig. 10(d)).

To correct for the first three components of E_n^t, as depicted in Fig. 10(e), (12) can be used to directly calculate fields (due to the source) at the output of the nth super slab. Here, the Green's function for a homogeneous medium with refractive index of n_{eff} is used. The obtained field is $E_n^{i,corrected} + < E_n^{s,corrected} > + < E_n^{s,c,corrected} >$.

Assuming the total fluctuating component of the scattered part of the input wave to the nth super slab, $\widetilde{E}_{(n-1)}^{s,t}$, is known, as illustrated in Fig. 10(f), (12) with the Green's function of a homogeneous medium with refractive index of n_{eff} can be used to find the fields at the output of the nth super slab due to $\widetilde{E}_{(n-1)}^{s,t}$. The result is the corrected $\widetilde{E}_n^s$ $(= \widetilde{E}_n^{s,corrected})$.

Finally, the corrected fields at the output of the nth super slab is $E_n^{\text{corrected}} = E_n^{i,corrected} + < E_n^{s,corrected} > + < E_n^{s,c,corrected} > + \widetilde{E}_n^{s,corrected} + \widetilde{E}_n^{s,c,corrected}$.

In the presented method, since the super slabs are not cascaded, interactions between the super slabs are not considered. To include a second order interaction between two adjacent super slabs for forward propagation wave, the method illustrated in Fig. 10(g) is used. The summation of corrected fields at the output of the nth super slab is expanded at the z^- interface of $(n+1)$th super slab and the resulting source vector is multiplied by the S-matrix of the $(n+1)$th super slab. The resulting backward propagating waves at z^- interface of the $(n+1)$th super slab represent the first order backscattered waves. The first order backscattered waves are then used as source at z^+ interface of nth super slab. The resulting forward propagating wave at z^+ interface of the nth super slab is the second order scattered wave and is denoted by $\widetilde{E}_{n,n+1}^{s,m}$. In this case, the total corrected field at the output of the nth super slab (input of $(n+1)$th super slab) is $E_n^{t,corrected} = E_n^{\text{corrected}} + \widetilde{E}_{n,n+1}^{s,m}$. The total fluctuating part, $\widetilde{E}_n^{s,t}$, is equal to $\widetilde{E}_n^{s,corrected} + \widetilde{E}_n^{s,c,corrected} + \widetilde{E}_{n,n+1}^{s,m}$ and will be used to calculate corrected $\widetilde{E}_{(n+1)}^s$ for the next super slab.

APPENDIX B
SCATTERING FROM A SPHERICAL SCATTERER

In this section, scattered field from a lossy dielectric sphere is calculated for an incident plane wave with arbitrary polarization and angle of incidence.

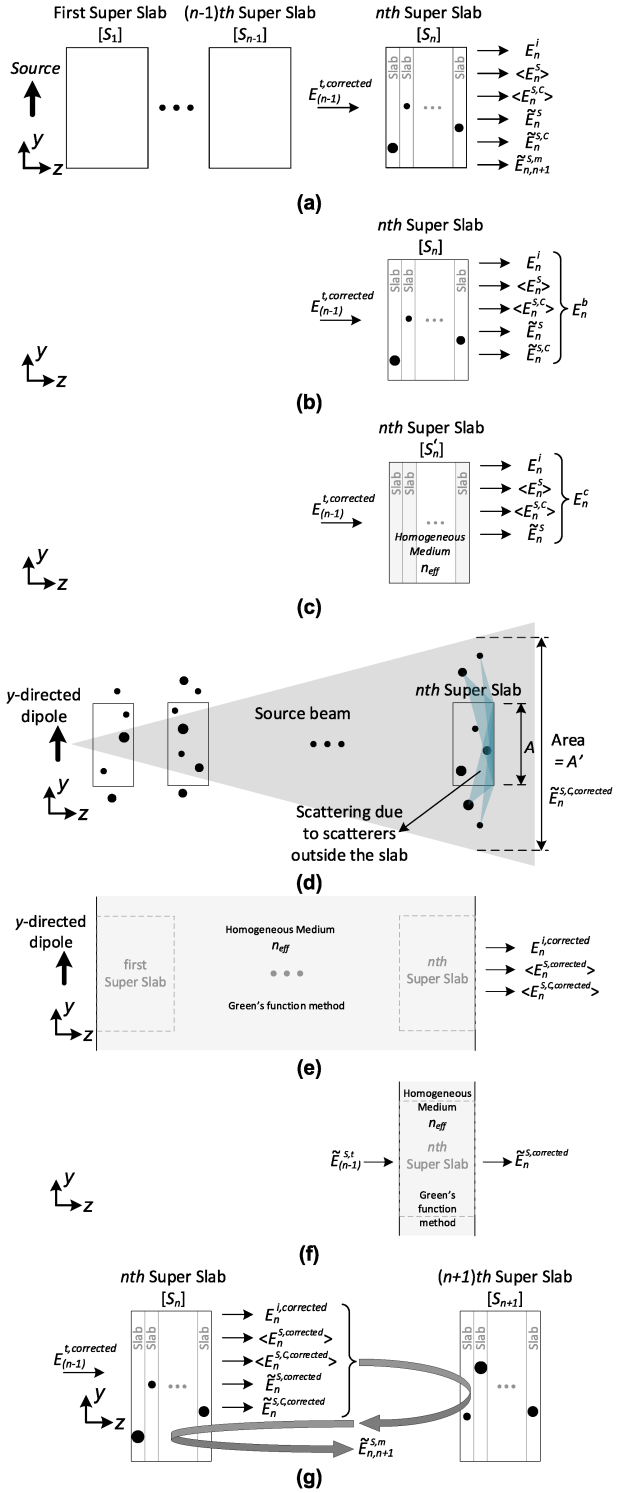

FIGURE 10. Correction scheme for S-matrix and Green's function method. (a) Components of forward propagating wave at the output of the *n*th super slab. (b) Extracting the first five components of (a). (c) Extracting the first four components of (a). (d) Scattering from the particles outside the slab. (e) Corrected E_n^i, $< E_n^s >$, and $< E_n^{s,c} >$. (f) Corrected $\tilde{E}_n^s$. (g) Calculating $\tilde{E}_{n,n+1}^{s,m}$.

Figure 11 shows the geometry of the problem. A dielectric and non-magnetic (permeability $= \mu_0$) sphere with complex dielectric constant of $\varepsilon = \varepsilon_s$ is considered in free space

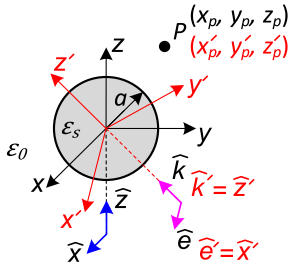

FIGURE 11. Sphere illuminated by a plane wave. Original coordinate system is denoted by (x, y, z) and rotated coordinate system in denoted by (x', y', z'). The plane wave used in (18) is shown in blue and the arbitrary plane wave is shown in pink. The arbitrary plane wave is defined by $\hat{k}$ and $\hat{e}$ in the original coordinate system and $\hat{k}' = \hat{z}'$ and $\hat{e}' = \hat{x}'$ in the rotated coordinate system.

($\varepsilon = \varepsilon_0$). The radius of the sphere is a and its center is located at the origin of a coordinate system. Assuming the sphere is illuminated by an incident plane wave with $\overline{k} = k_0\hat{z}$ (k_0 is the propagation constant in free space at angular frequency ω) and $\overline{E} = 1e^{-jk_0z}\hat{x}$, the scattered electric field components at a desired coordinate ($r > a$, θ, ϕ) are [33]:

$$\begin{cases} E_r^s = \frac{k_0}{\omega\mathrm{r}}\cos(\phi)\sum_{n=1}^{\infty}\left(n(n+1)a_n\frac{\hat{h}_n^{(2)}(k_0r)}{k_0r}P_n^1(\cos(\theta))\right) \\ E_\theta^s = \cos(\phi)\sum_{n=1}^{\infty}\left(\begin{matrix} ja_n\frac{\hat{h}_n^{(2)'}(k_0r)}{k_0r}\sin(\theta)P_n^{1'}(\cos(\theta)) \\ -b_n\frac{\hat{h}_n^{(2)}(k_0r)}{k_0r}\frac{P_n^1(\cos(\theta))}{\sin(\theta)} \end{matrix}\right) \\ E_\phi^s = \sin(\phi)\sum_{n=1}^{\infty}\left(\begin{matrix} ja_n\frac{\hat{h}_n^{(2)'}(k_0r)}{k_0r}\frac{P_n^1(\cos(\theta))}{\sin(\theta)} \\ -b_n\frac{\hat{h}_n^{(2)}(k_0r)}{k_0r}\sin(\theta)P_n^{1'}(\cos(\theta)) \end{matrix}\right), \end{cases} \tag{18}$$

where $\hat{h}_n^{(2)}$ is Schelkunoff spherical Hankel function of second kind and order n, P_n^1 is the associated Legendre function of degree n and order 1, the primes indicate the first derivative of the function with respect to its argument, and a_n and b_n are given by:

$$\begin{cases} a_n = \frac{(-j)^n(2n+1)}{n(n+1)} \\ \quad \times \frac{-\sqrt{\varepsilon_s/\varepsilon_0}\hat{j}_n'(k_0a)\hat{j}_n(k_sa)+\hat{j}_n(k_0a)\hat{j}_n'(k_sa)}{\sqrt{\varepsilon_s/\varepsilon_0}\hat{h}_n^{(1)'}(k_0a)\hat{j}_n(k_sa)+\hat{h}_n^{(1)}(k_0a)\hat{j}_n'(k_sa)} \\ b_n = \frac{(-j)^n(2n+1)}{n(n+1)} \\ \times \frac{-\sqrt{\varepsilon_s/\varepsilon_0}\hat{j}_n(k_0a)\hat{j}_n'(k_sa)+\hat{j}_n'(k_0a)\hat{j}_n(k_sa)}{\sqrt{\varepsilon_s/\varepsilon_0}\hat{h}_n^{(1)}(k_0a)\hat{j}_n'(k_sa)-\hat{h}_n^{(1)'}(k_0a)\hat{j}_n(k_sa)}. \end{cases} \tag{19}$$

In (19), $\hat{j}_n$ is Schelkunoff spherical Bessel function of first kind and order n and $k_s = \omega\sqrt{\mu_0\varepsilon_s}$.

To find the scattered fields due to a general plane wave propagating in $\hat{k}$ ($= k_x\hat{x}+k_y\hat{y}+k_z\hat{z}$) direction with the electric field $\overline{E} = 1\hat{e}e^{-jk_0r}$ ($\hat{e}$ and $\hat{k}$ are unit vectors and $\hat{e}\cdot\hat{k} = 0$) at a point P defined by (x_p, y_p, z_p), the following steps are followed:

1) As shown in Fig. 11, the coordinate system must be rotated such that in the new coordinate (defined by orthonormal vectors $\hat{x}'$, $\hat{y}'$, and $\hat{z}'$) $\hat{z}'$ is aligned with $\hat{k}$ and $\hat{x}'$ is aligned with $\hat{e}$. The point P in the new

rotated coordinate, (x_p', y_p', z_p'), is defined by:

$$\begin{pmatrix} x_p' \\ y_p' \\ z_p' \end{pmatrix} = \underbrace{\begin{pmatrix} \hat{e}\cdot\hat{x} & \hat{e}\cdot\hat{y} & \hat{e}\cdot\hat{z} \\ (\hat{k}\times\hat{e})\cdot\hat{x} & (\hat{k}\times\hat{e})\cdot\hat{y} & (\hat{k}\times\hat{e})\cdot\hat{z} \\ \hat{k}\cdot\hat{x} & \hat{k}\cdot\hat{y} & \hat{k}\cdot\hat{z} \end{pmatrix}}_{\bar{\bar{R}}} \begin{pmatrix} x_p \\ y_p \\ z_p \end{pmatrix}. \tag{20}$$

In (20), $\bar{\bar{R}}$ is the rotation matrix and all the parameters on the right-hand side are in the original coordinate system.

2) Using (18), the scattered fields can be calculated at (x_p', y_p', z_p') in the rotated coordinate. The obtained scattered field components in the rotated coordinate system are denoted by $(E_x^{s'}, E_y^{s'}, E_z^{s'})$.

The scattered field components in the original coordinate system, (E_x^s, E_y^s, E_z^s), are obtained by:

$$\begin{pmatrix} E_x^s \\ E_x^s \\ E_x^s \end{pmatrix} = \bar{\bar{R}}^T \begin{pmatrix} E_x^{s'} \\ E_y^{s'} \\ E_z^{s'} \end{pmatrix}, \tag{21}$$

where $\bar{\bar{R}}^T$ is the transpose of $\bar{\bar{R}}$.

REFERENCES

[1] T. S. Rappaport, Y. Xing, G. R. MacCartney, A. F. Molisch, E. Mellios, and J. Zhang, "Overview of millimeter wave communications for fifth-generation (5G) wireless networks—With a focus on propagation models," *IEEE Trans. Antennas Propag.*, vol. 65, no. 12, pp. 6213–6230, Dec. 2017.

[2] L. Chettri and R. Bera, "A comprehensive survey on Internet of Things (IoT) toward 5G wireless systems," *IEEE Internet Things J.*, vol. 7, no. 1, pp. 16–32, Jan. 2020.

[3] S. Sun, A. P. Petropulu, and H. V. Poor, "MIMO radar for advanced driver-assistance systems and autonomous driving: Advantages and challenges," *IEEE Signal Process. Mag.*, vol. 37, no. 4, pp. 98–117, Jul. 2020.

[4] K. Sarabandi, A. Jam, M. Vahidpour, and J. East, "A novel frequency beam-steering antenna array for submillimeter-wave applications," *IEEE Trans. THz Sci. Technol.*, vol. 8, no. 6, pp. 654–665, Nov. 2018.

[5] A. Alaqeel, A. A. Ibrahim, A. Nashashibi, H. Shaman, and K. Sarabandi, "Experimental characterization of multi-polarization radar backscatter response of vehicles at *J*-band," *IEEE Trans. Intell. Transp. Syst.*, vol. 20, no. 9, pp. 3337–3350, Sep. 2019.

[6] F. Wang and K. Sarabandi, "An enhanced millimeter-wave foliage propagation model," *IEEE Trans. Antennas Propag.*, vol. 53, no. 7, pp. 2138–2145, Jul. 2005.

[7] S. Joshi and S. Sancheti, "Foliage loss measurements of tropical trees at 35 GHz," in *Proc. Int. Conf. Recent Adv. Microw. Theory Appl.*, 2008, pp. 531–532.

[8] T. E. Bogale, X. Wang, and L. B. Le, "mmWave communication enabling techniques for 5G wireless systems: A link level perspective," in *mmWave Massive MIMO*, Cambridge, MA, USA: Academic Press, 2017, ch. 6.

[9] M. Rangwala, F. Wang, and K. Sarabandi, "Study of millimeter-wave radar for helicopter assisted-landing system," *IEEE Antennas Propag. Mag.*, vol. 50, no. 2, pp. 13–25, Apr. 2008.

[10] M. R. Akdeniz et al., "Millimeter wave channel modeling and cellular capacity evaluation," *IEEE J. Sel. Areas Commun.*, vol. 32, no. 6, pp. 1164–1179, Jun. 2014.

[11] T. S. Rappaport, G. R. MacCartney, M. K. Samimi, and S. Sun, "Wideband millimeter-wave propagation measurements and channel models for future wireless communication system design," *IEEE Trans. Commun.*, vol. 63, no. 9, pp. 3029–3056, Sep. 2015.

[12] H. Zhao et al., "28 GHz millimeter wave cellular communication measurements for reflection and penetration loss in and around buildings in New York city," in *Proc. IEEE Int. Conf. Commun. (ICC)*, 2013, pp. 5163–5167.

[13] I. Shayea, T. A. Rahman, M. Hadri Azmi, and A. Arsad, "Rain attenuation of millimetre wave above 10 GHz for terrestrial links in tropical regions," *Wiley Trans. Emerg. Telecommun. Technol.*, vol. 29, no. 8, Aug. 2018, Art. no. e3450.

[14] S. Shrestha and D.-Y. Choi, "Rain attenuation statistics over millimeter wave bands in South Korea," *J. Atmos. Solar-Terr. Phys.*, vol. 152, pp. 1–10, Jan. 2017.

[15] J. S. Marshall and W. M. Palmer, "The distribution of raindrops with size," *J. Meteorol.*, vol. 5, no. 4, pp. 165–166, 1948.

[16] C. W. Ulbrich, "Natural variations in the analytical form of the raindrop size distribution," *J. Climate Appl. Meteorol.*, vol. 22, no. 10, pp. 1764–1775, Oct. 1983.

[17] L. L. Foldy, "The multiple scattering of waves," *Phys. Rev.*, vol. 67, no. 3, pp. 107–119, Feb. 1945.

[18] L. Tsang, J. A. Kong, and K.-H. Ding, *Scattering of Electromagnetic Waves: Theories and Applications*, New York, NY, USA: Wiley, 2000.

[19] K. Sarabandi, A. Tavakoli, and F. T. Ulaby, "Propagation in a two-dimensional periodic random medium with inhomogeneous particle distribution," *IEEE Trans. Antennas Propag.*, vol. 40, no. 10, pp. 1175–1186, Oct. 1992.

[20] P. R. Siqueira and K. Sarabandi, "T-matrix determination of effective permittivity for three-dimensional dense random media," *IEEE Trans. Antennas Propag.*, vol. 48, no. 2, pp. 317–327, Feb. 2000.

[21] W. Zhensen, Y. Yi, and C. Lihong, "Monte Carlo simulation for millimeter wave propagation and scattering in rain medium," *Int. J. Infrared Millimeter Waves*, vol. 13, no. 7, pp. 981–994, 1992.

[22] F. Wang and K. Sarabandi, "A physics-based statistical model for wave propagation through foliage," *IEEE Trans. Antennas Propag.*, vol. 55, no. 3, pp. 958–968, Mar. 2007.

[23] A. A. Ibrahim and K. Sarabandi, "Simulation of long distance wave propagation in 2-D sparse random media: A statistical S-matrix approach in spectral domain," *IEEE Trans. Antennas Propag.*, vol. 62, no. 5, pp. 2708–2720, May 2014.

[24] G. R. Simpson, "A generalized n-port cascade connection," in *Proc. IEEE MTT-S Int. Microw. Symp. Dig.*, 1981, pp. 507–509.

[25] S. Ermis, "A microwave backscattering model for precipitation," Ph.D. dissertation, Dept. Elect. Eng., Univ. Texas at Arlington, Arlington, TX, USA, 2015.

[26] F. T. Ulaby and D. G. Long, "Microwave dielectric properties of natural earth materials," in *Microwave Radar and Radiometric Remote Sensing*. Ann Arbor, MI, USA: Univ. Michigan Press, 2017, ch. 4.

[27] *Attenuation by Hydrometeors, in Particular Precipitation, and Other Atmospheric Particles*, CCIR document 721-3, ITU, Geneva, Switzerland, 1990.

[28] T. Manabe, T. Ihara, J. Awaka, and Y. Furuhama, "The relationship of raindrop-size distribution to attenuations experience at 50, 80, 140, and 240 GHz," *IEEE Trans. Antennas Propag.*, vol. 35, no. 11, pp. 1326–1330, Nov. 1987.

[29] J. R. Norbury and W. J. K. White, "Microwave attenuation at 35 8 GHz due to rainfall," *Electron. Lett.*, vol. 8, no. 4, pp. 91–92, Feb. 1972.

[30] J. Sander, "Rain attenuation of millimeter waves at $\lambda = 5.77$, 3.3, and 2 mm," *IEEE Trans. Antennas Propag.*, vol. 23, no. 2, pp. 213–220, Mar. 1975.

[31] Y. Furuhama and T. Ihara, "Remote sensing of path-averaged raindrop size distributions from microwave scattering measurements," *IEEE Trans. Antennas Propag.*, vol. 29, no. 2, pp. 275–281, Mar. 1981.

[32] A. Hirata et al., "Effect of rain attenuation for a 10-Gb/s 120-GHz-band millimeter-wave wireless link," *IEEE Trans. Microw. Theory Techn.*, vol. 57, no. 12, pp. 3099–3105, Dec. 2009.

[33] K. Sarabandi, "Spherical wave functions and their applications," in *Foundations of Applied Electromagnetics*, Ann Arbor, MI, USA: Michigan Publ., 2022.

BEHZAD YEKTAKHAH (Member, IEEE) received the B.S. and M.S. degrees in electrical engineering from the University of Tehran, Tehran, Iran, in 2008 and 2011, respectively, and the Ph.D. degree in electrical engineering from the University of Michigan at Ann Arbor in 2019.

He is currently a Postdoctoral Research Fellow with the University of Michigan at Ann Arbor. His research focuses on radar imaging, electromagnetic scattering, antennas, and phased arrays.

KAMAL SARABANDI (Life Fellow, IEEE) is currently the Fawwaz T. Ulaby Distinguished University Professor and the Rufus S. Teesdale Endowed Professor of Engineering with the University of Michigan at Ann Arbor, Ann Arbor, MI, USA. He led the Center for Microelectronics and Sensors funded by the Army Research Laboratory from 2008 to 2018 and has been leading the Center of Excellence in Microwave Sensor Technology. He has supervised 63 Ph.D. and numerous master's students and postdoctoral fellows. He has published many book chapters, more than 325 articles in refereed journals, and more than 770 conference papers. His research interests include microwave and millimeter-wave radar remote sensing, metamaterials, electromagnetic wave propagation, antenna miniaturization, and bioelectromagnetics. He, together with his students, was a recipient of 35 paper awards. His contributions to the field of electromagnetics have been recognized by many awards, including the Humboldt Research Award, the IEEE GRSS Distinguished Achievement Award, the IEEE Judith A. Resnik Medal, the IEEE GRSS Education Award, the NASA Group Achievement Award, and many other awards from the University of Michigan at Ann Arbor. He was the Chair of Commission F of USNC/URSI and has been serving as a member of the AdCom for the IEEE Antennas and Propagation Society. He is a member of the National Academy of Engineering. He has served as a member of the NASA Advisory Council for two consecutive terms from 2006 to 2010 and the President of the IEEE Geoscience and Remote Sensing Society from 2015 to 2016. He is a Fellow of the American Association for the Advancement of Science and the National Academy of Inventors.